JOURNAL OF GEOPHYSICAL RESEARCH, VOL. 112, B04312, doi:10.1029/2006JB004449, 2007

Upper mantle structure of South America from joint inversion of waveforms and fundamental mode group velocities of Rayleigh waves

Mei Feng,[1,2] Suzan van der Lee,[3] and Marcelo Assumpção[1]

Received 14 April 2006; revised 4 October 2006; accepted 30 November 2006; published 27 April 2007.

[1] A new tomographic *S* wave velocity model for the upper mantle beneath South America is presented. We developed and applied a new method of simultaneously inverting regional *S* and Rayleigh waveforms and fundamental mode Rayleigh wave group velocities, to better constrain upper mantle *S* velocity structure and Moho depth. We used ~5700 Rayleigh wave group velocity dispersion curves and 1537 regional wave trains with paths principally passing through the South American continent. The joint inversion of this data set provided a new three-dimensional (3-D) upper mantle *S* velocity model and a Moho depth model for South America, which fits both the group velocity and regional waveform data sets well. New features of the final three-dimensional (3-D) *S* velocity and Moho depth model correlate well with known geotectonic units on a regional scale. The Moho depth ranges from 30 km in the central Chaco basin to 42 km beneath the Amazonian craton and 45–70 km beneath the orogenic Andean belt. The imaged *S* velocity indicates an average lithosphere thickness of around 160 km for the Amazonian craton. High velocities are imaged beneath the Amazon and part of the Paraná and Parnaíba basins down to about 150 km. Low to very low velocities are imaged beneath the central Andes and the Chaco, Pantanal, and northwestern Paraná basins.

Citation: Feng, M., S. van der Lee, and M. Assumpção (2007), Upper mantle structure of South America from joint inversion of waveforms and fundamental mode group velocities of Rayleigh waves, *J. Geophys. Res.*, *112*, B04312, doi:10.1029/2006JB004449.

1. Introduction

[2] South America is characterized by diverse tectonic environments (Figure 1a). The large Precambrian stable South American Platform, composed of shields, cratons, mobile belts and sedimentary basins, forms the tectonic core of the continent. The younger Patagonian Platform to the south stems from the late Paleozoic. The active Andean orogenic belt bounds the western coast.

[3] The South American Platform (Figure 1a) contains the Guyana shield in the north, Guaporé shield in the center, and São Francisco craton in the southeast, as well as buried Precambrian basement beneath the Amazon basin in the north, Parnaíba basin in the northeast, and Paraná basin in the south, and beneath the Sub-Andean Foredeep to the west and Atlantic coastal margin deposits to the east [*Almeida et al.*, 2000; *Goodwin*, 1991]. The Guyana and the Guaporé shields, surficially separated by the Amazon basin, form the Amazonian craton, one of the largest and least known Archean-Proterozoic areas in the world. The Amazonian craton contains six main geochronological provinces as shown in Figure 1b [*Santos et al.*, 2000; *Tassinari and Macambira*, 1999]. The Archean protocraton of the Amazonian craton consisted formerly of independent microcontinents that were amalgamated by Paleoproterozoic orogenic belts between 2.2 and 1.95 Ga. Part of the Maroni–Itacaiúnas province (MIP in Figure 1b) and Rondônia–San Ignácio province (RSIP), and the whole Ventuari-Tapajós province (VTP) and Rio Negro–Juruera province (RNJP) evolved by addition of juvenile magmas to the crust from 1.95 to 1.4 Ga, while the crustal evolution of the Sunsás province (SP) and part of Maroni-Itacaiúnas province and Rondônia–San Ignácio province is associated with later reworking of Paleoproterozoic and Mesoproterozoic continental crust [*Tassinari and Macambira*, 1999]. The São Francisco craton involves an Archean nucleus surrounded by Paleoproterozoic terranes [*Teixeira et al.*, 2000]. On both cratons, crustal evolution was similar between 3.0 and 1.7 Ga, suggesting that they were possibly contiguous, within a Paleoproterozoic supercontinent [*Cordani and Sato*, 1999]. The continental-scale, NE–SW trending Transbrasiliano lineament (TBL in Figure 1a) marks the weak zone between these two main cratons.

[4] The Andean mountain chain along the western continental margin resulted from the former Farallon plate and the present Nazca plate subducting beneath the South American plate. The present subduction geometry beneath the Andean cordillera is characterized by the along-strike variation in dip of the subducting Nazca plate from subhorizontal flat slab segments to normal subduction [*Cahill and Isacks*, 1992; *Ramos*, 1999]. Normal subduction dipping around 30° occurs in the central section of the central

[1]Department of Geophysics, Institute of Astronomy, Geophysics and Atmospheric Sciences, University of São Paulo, São Paulo, Brazil.
[2]Now at Institute of Geomechanics, Chinese Academy of Geological Sciences, Beijing, China.
[3]Department of Geological Sciences, Northwestern University, Evanston, Illinois, USA.

0148-0227/07/2006JB004449$09.00

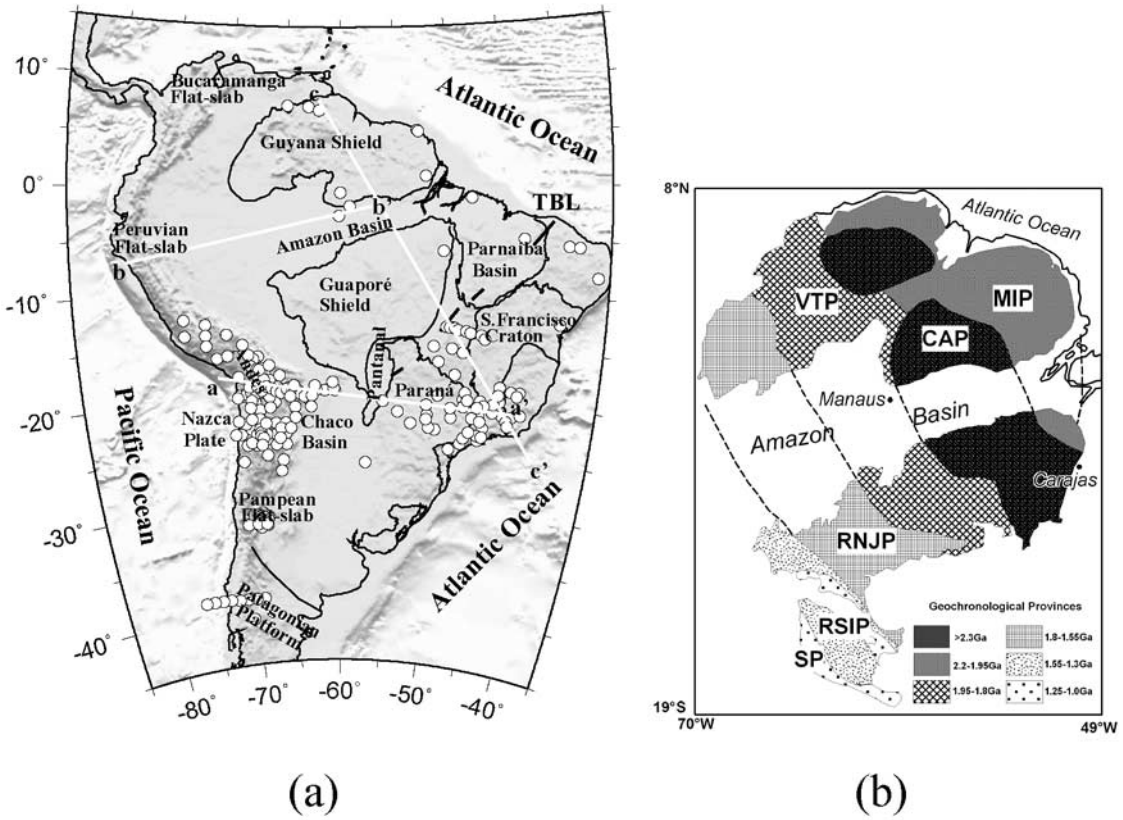

Figure 1. (a) Simplified geotectonic map of South America. White circles indicate locations of a priori constraints of crust thickness. The profiles aa'–cc' are in the present study. Thick dashed line labeled with "TBL" is the surface expression of the Transbrasiliano lineament. (b) Simplified map of geochronological provinces of the Amazonian craton based on the work by *Tassinari and Macambira* [1999]. CAP indicates the Central Amazonian Province, older than 2.3 Ga; MIP is the Maroni-Itacaiúnas province, 2.2–1.95 Ga; VTP is the Ventuari-Tapajós province, 1.95–1.8 Ga; RNJP is the Rio Negro–Juruena province, 1.8–1.55 Ga; RSIP is the Rondônia–San Ignácio province, 1.5–1.3 Ga; and SP is the Sunsás province, 1.25–1.00 Ga. Carajás is the location near the oldest Archean granitoids found in the South American continent.

Andes between 14°S and 27°S and flat subduction dipping about 5° takes place north and south of the central section, between 5°S and 14°S and between 27°S and 33°S, respectively. The former corresponds to the Peruvian flat slab segment and the latter to the Pampean flat slab segment. In the northern Andes, north of 5°N, there is another flat slab segment, called Bucaramanga segment [*Cahill and Isacks*, 1992; *Pennington*, 1981; *Ramos*, 1999]. Regions above the three mentioned flat slab segments are characterized by high seismic energy release and lack of active volcanism compared to the normal subduction regions [*Gutscher and Malavieille*, 1999; *Ramos*, 1999].

[5] The dominant features of South America imaged by global tomographic studies [*Boschi and Ekström*, 2002; *Ekström and Dziewonski*, 1998; *Grand*, 1994; *Larson and Ekström*, 2001; *Laske and Masters*, 1996; *Mégnin and Romanowicz*, 2000; *Ritzwoller et al.*, 2002; *Shapiro and Ritzwoller*, 2002; *Trampert and Woodhouse*, 1995; *Woodhouse and Dziewonski*, 1984; Colorado Group, 2004, http://ciei.colorado.edu/~nshapiro/MODEL] are the high-velocity lithospheric continental roots in the northern and central South America and the low-velocity plate boundaries along the western continental margin. All but the model of the Colorado Group (2004, http://ciei.colorado.edu/~nshapiro/MODEL) can hardly detect the different provinces inside the stable platform, or the subhorizontal subduction segments along the Andes, because of their long-wavelength resolution (> ~10°). The model of the Colorado Group shows some regional features, such as the low velocities down to 200 km beneath the Chaco and Pantanal basins and two separate high-velocity regions at 200 km correlating to the Amazonian and the São Francisco cratons. These features are in general agreement with the regional models of *van der Lee et al.* [2001] and *Feng et al.* [2004] but with different anomaly amplitude and extent.

[6] Most of the regional studies in South America have focused on some specific regions of the Andean subduction zone to characterize the subducting Nazca slab and the mantle wedge [*Dorbath and Masson*, 2000; *Engdahl et al.*, 1995; *Haberland and Rietbrock*, 2001; *James and Snoke*, 1990; *Myers et al.*, 1998; *Schneider and Sacks*, 1987] without or with limited coverage of the stable South American platform. Some local tomographic studies have been carried out in SE Brazil, to study the Paraná basin and its surrounding fold belts [*Assumpção et al.*, 2004b; *Schimmel et al.*, 2003; *VanDecar et al.*, 1995]. Only a few

tomographic studies for South America covered the stable platform [*Feng et al.*, 2004; *Heintz et al.*, 2005; *Silveira and Stutzmann*, 2002; *Silveira et al.*, 1998; *van der Lee et al.*, 2001; *Vdovin et al.*, 1999]. Both the fundamental mode based [*Feng et al.*, 2004; *Silveira et al.*, 1998; *Vdovin et al.*, 1999] and the multimode based [*Heintz et al.*, 2005; *van der Lee et al.*, 2001] tomography studies have mapped common large-scale features in South America. However, these previous tomographic studies have limited lateral resolution because of either poor path coverage [*van der Lee et al.*, 2001] or very long paths and long periods [*Heintz et al.*, 2005; *Silveira et al.*, 1998]. Limited depth sensitivity below 150 km is a problem for models using only fundamental mode surface waves [*Feng et al.*, 2004; *Vdovin et al.*, 1999].

[7] Inversion methods using only waveforms have good sensitivity to deep structures because several multimode branches can be included, but the path coverage tends to be limited by the few large events with well-determined focal mechanisms (mb > 5.5). The combination of fundamental mode dispersion (better path coverage from more events) and multimode waveforms (better depth sensitivity from the higher modes) should improve both the lateral and depth resolution of the tomographic model. Inversion of multidata sets is becoming increasingly important in geophysical studies to compensate the deficiency caused by isolated data sets [*An and Assumpção*, 2004; *Ritsema et al.*, 2004; C. Schmid et al., Three-dimensional *S* velocity model beneath the Mediterranean region to 1400 km from joint inversion of teleseismic arrival times and regional waveform fits, submitted to *Journal of Geophysical Research*, 2005].

[8] The present work is an effort to incorporate both multimode Rayleigh waveforms and fundamental mode group velocities into surface wave tomography, to determine a 3-D upper mantle *S* velocity and Moho depth model for South America. Unlike the usual group velocity tomography correcting for crustal effects with an a priori crustal depth model, such as CRUST5.1 [*Mooney et al.*, 1998] or 3SMAC [*Nataf and Richard*, 1996], we inverted simultaneously for Moho depth and *S* velocity by including partial derivatives of group velocity to Moho depth ($\partial U/\partial H$) as well as those of waveforms to Moho depth. Besides this improvement in inversion technique, we also installed new seismic stations [*Feng et al.*, 2004] and so collected a large data set with the best path coverage to date for the stable part of the South American continent. We augment the inversion with independent point constraints on crustal thickness as in the work by *van der Lee et al.* [2001].

2. Data

[9] Our model is based on two types of data: fundamental mode Rayleigh wave group velocities and multimode Rayleigh wave trains. Rayleigh wave seismograms have been recorded by GSN and GEOSCOPE permanent stations, mainly located in the South America continent and a few in its surrounding ocean islands, and by temporary broadband stations deployed in SE Brazil by BLSP92 [*James et al.*, 1993] and BLSP95 [*Assumpção et al.*, 2002], and NE Brazil by BLSP02 [*Feng et al.*, 2004] experiments with operation between 1992 and 2004. We used earthquakes through May 2004 and preferentially selected pure continental paths for analysis which yields ~5700 dispersion curves. The earthquakes, stations and raypaths for the group velocity data are shown in Figure 2a. In addition, we collected a total of 1537 regional wave trains, mostly from the same data bank. Among them, about 1100 were analyzed in this study, and the other 440 waveforms, from 1992 to 1996, had been fit for model SA99 [*van der Lee et al.*, 2001], which included data from the BANJO experiment in Bolivia [*Beck et al.*, 1996] and VEN92 in Venzuela [*Russo et al.*, 1996]. The path coverage for the 1537 regional waveforms (Figure 2b) constitutes a drastic improvement over that used for SA99 [*van der Lee et al.*, 2001]. As we determine not only *S* velocity but also Moho depth, we also collected 229 point constraints of crustal thickness from previous receiver function analysis and seismic refraction/reflection studies [*Crotwell and Owens*, 2005; *França and Assumpção*, 2004; *Krüger et al.*, 2002; *Schmitz et al.*, 2002]. The distribution of these point constraints is indicated with white circles in Figure 1a.

[10] All of our group velocity measurements have been performed using the codes of R. B. Herrmann and C. J. Ammon (Computer programs in seismology: Surface waves, receiver functions and crustal structure, St. Louis University, 2002, available at http://www.eas.slu.edu/People/RBHerrmann/CPS330.html), as explained in detail by *Feng et al.* [2004]. For the group velocity measurements, only hypocenter location and origin time (taken from EHB catalogues [*Engdahl et al.*, 1998]) are needed, which permits the use of relatively small events (mb > 4.5). Synthetic waveform calculation, on the other hand, requires the earthquake moment tensor solution, which limits its application to relatively large events (mb > 5.5). So, from the same data bank, we retrieved fewer Rayleigh waveforms than group velocity dispersion curves (Figure 2). The Rayleigh waveforms were processed with the PWI package of *van der Lee and Nolet* [1997]. For the synthetic waveform calculation, the hypocenter locations and origin times were taken from the NEIC catalogue and moment tensor solutions from the Harvard Centroid Moment Tensor (CMT) catalogue [*Dziewonski et al.*, 1983]. For each vertical component displacement seismogram, one or two time windows of waveforms were fit, encompassing the fundamental mode Rayleigh wave as well as all (multiple) *S* waves with turning points within the upper mantle.

3. Method

[11] Our tomography from joint inversion of fundamental mode group velocities and full regional waveforms is developed on the base of their independent inversions. The inversion of group velocities for a 3-D *S* velocity model is normally broken into two steps: (1) the estimation of group velocity maps at different periods and (2) the inversion of each regionalized group velocity dispersion for 1-D *S* velocity model, which comprise the final 3-D model [*Feng et al.*, 2004; *Pasyanos et al.*, 2001; *Ritzwoller and Levshin*, 1998; *Villaseñor et al.*, 2001]. The PWI method [*van der Lee and Nolet*, 1997] is also done in two steps: (1) nonlinear waveform fitting to determine 1-D average *S* velocity structure and Moho depth along each path and (2) linear inversion of all 1-D path-averaged structures and independent point constraints of Moho depth to get the 3-D model of *S* velocity and Moho depth. Our joint inversion of

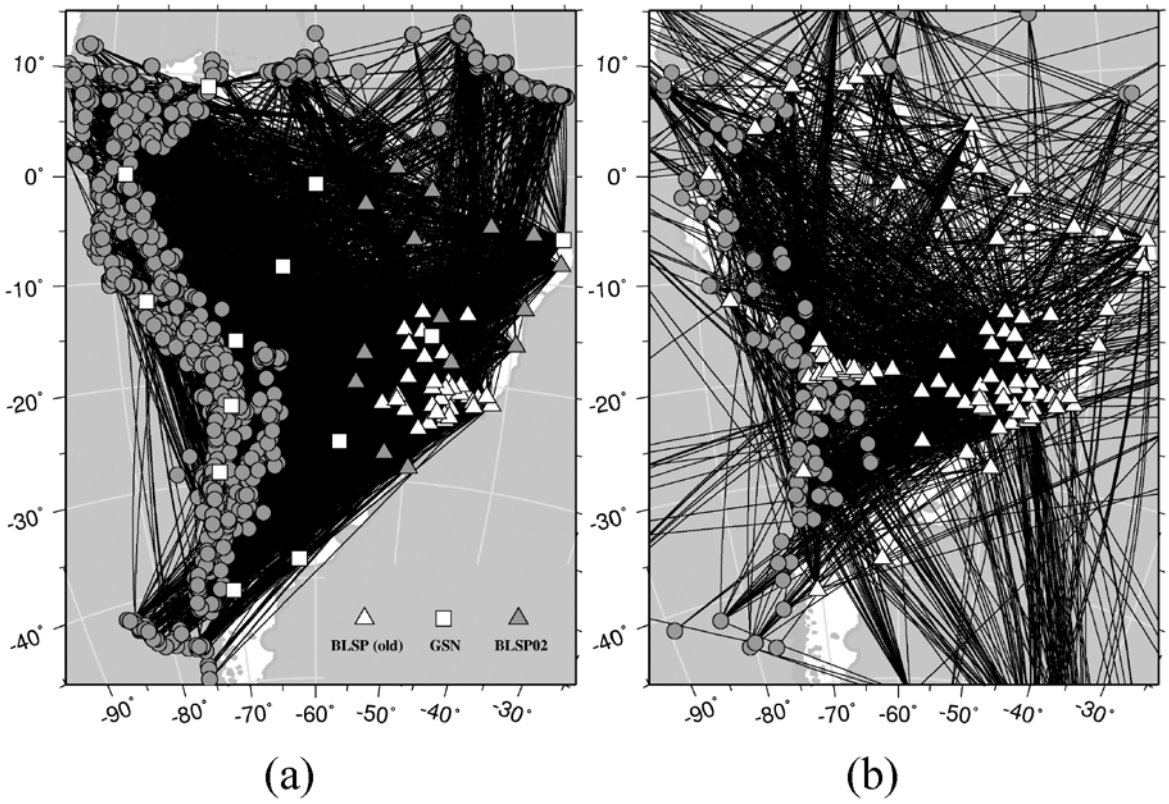

Figure 2. (a) Seismic stations (triangles and squares), earthquakes (circles), and 5700 great circle raypaths (black lines) used for Rayleigh wave group velocity tomography at 30 s period. (b) 1537 raypaths for Rayleigh waveform data.

group velocities and waveforms differs from the independent inversions only in the second step, which determines the 3-D *S* velocity model and Moho depth by combining the regionalized dispersion curves (results of the first step of group velocity tomography), and the 1-D path-averaged structures (results of the first step of PWI).

[12] Both the linear inversion of regionalized group velocities and inversion of 1-D path-averaged structure for a 3-D model can be expressed in a matrix form as

$$\begin{pmatrix} \mathbf{H} \\ \lambda \mathrm{I} \end{pmatrix} \mathbf{m} = \begin{pmatrix} \mathbf{q} \\ \mathbf{0} \end{pmatrix} \tag{1}$$

where **H** is sensitivity matrix, **q** is data vector, **m** are 3-D model parameters to be estimated. λ determines the strength of damping. However, for inversions of different constraints, **H** and **q** have different entries.

[13] For the inversion of linear constraints from waveform modeling, 1-D path-averaged *S* velocities and Moho depths are first determined from waveform fitting [*van der Lee and Nolet*, 1997] and then expressed in the form of linear constraints with uncorrelated uncertainties in the 3-D linear inversion. So **H** in equation (1) is a matrix with entries of path-related coefficients, **q** is a data vector related to path-averaged structure; and **m** represents perturbations of *S* velocity ($\Delta\beta$) and Moho depth (ΔH) relative to a given reference model to be determined. Here, we chose a reference model (SA40) similar to iasp91 [*Kennett and Engdahl*, 1991] but with a crustal thickness of 40 km, the average crustal thickness for the stable South American continent inferred from *Assumpção et al.* [2002]. The 3-D *S* velocity model is parameterized as coefficients of a Cartesian grid of nodes with 90 km, 90 km and 50 km of grid spacing in x, y and z direction, respectively. In fact, in equation (1), **H** includes both path constraints and model smoothing constraints by the way described by *van der Lee and Nolet* [1997]. Model smoothing has been built into 3-D linear inversion so that a smooth model can be obtained since no other a priori constraints are available.

[14] For the inversion of regionalized group velocities, group velocity tomography is first carried out on a 1° by 1° geographical grid, different from the Cartesian grid used in PWI. Partial derivatives of regionalized group velocities to *S* velocities ($\partial U/\partial\beta$) and to Moho depths ($\partial U/\partial H$) are then calculated for the same reference model SA40, consisting of horizontal layers of 20 km thickness. To convert the model parameterization of geographical grid to the Cartesian grid used in PWI, we introduced geometrical transforming coefficients into the group velocity derivatives. So, for group velocity inversion, **H** in equation (1) is a matrix with entries of group velocity partial derivatives times geometrical transforming coefficients, **q** is a data vector of group velocity difference between the regionalized and predicted group velocities (ΔU), and **m** is the same 3-D Cartesian model as the PWI model that includes perturbations of *S* velocity ($\Delta\beta$) and Moho depth (ΔH).

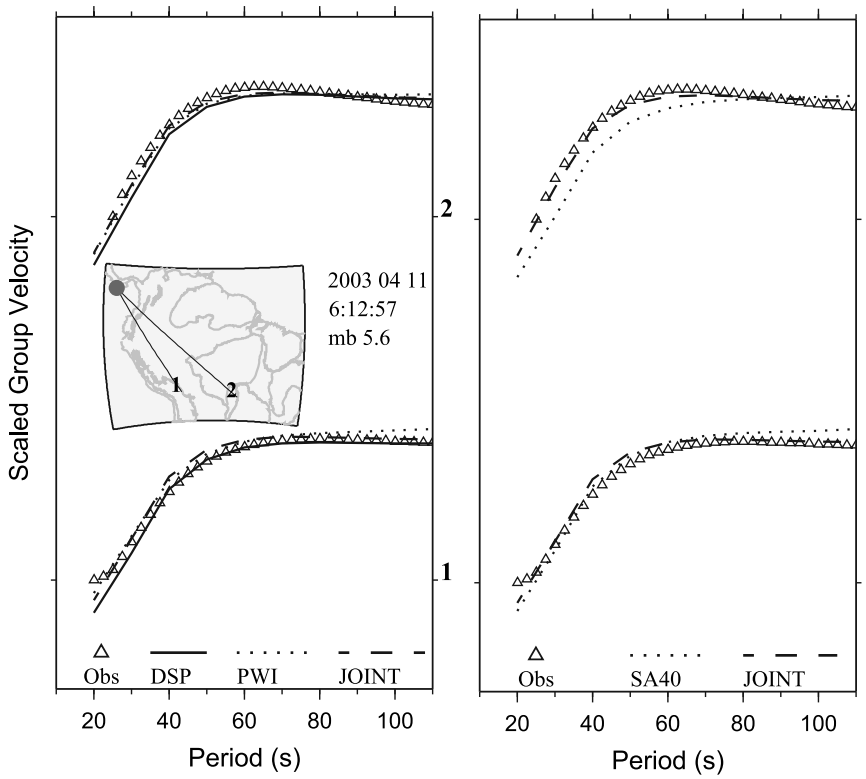

Figure 3. Fits between the observed and predicted group velocity dispersion curves of different models. (left) Comparison of the group velocity fits among the DSP, PWI, and JOINT models. (right) Comparison of the group velocity fits between the JOINT and SA40 models.

[15] For the joint inversion of waveform and regionalized dispersions, we use the same model parameterization and reference model as that used in PWI. So, we simply need combine the two sets of constraints as the following form:

$$\begin{pmatrix} \mathbf{H_w} \\ \lambda_d \mathbf{H_d} \\ \lambda \mathbf{I} \end{pmatrix} \mathbf{m} = \begin{pmatrix} \mathbf{q_w} \\ \lambda_d \mathbf{q_d} \\ \mathbf{0} \end{pmatrix} \tag{2}$$

where the subscripts w and d represent constraints of waveforms and dispersions, respectively. Besides the damping factor λ, we introduced a new factor λ_d to balance the weight between the constraints of waveforms and dispersions. That is, larger λ_d means more constraints of dispersions in the joint inversion. Both λ and λ_d are determined by trial tests so that the final 3-D model can fit both waveforms and dispersions reasonably well. As we simultaneously invert for two parameters in different units (i.e., perturbations of S velocity $\Delta\beta$ and Moho depth ΔH), two different column scaling factors (σ_β and σ_H) are introduced to the form of the sensitivity matrix $\mathbf{H}$ to normalize the parameters (i.e., $\Delta_\beta/\sigma_\beta$ and Δ_H/σ_H). These two factors also serve as weight to balance the inversion for S velocities and for Moho depth. These factors are also determined by trial tests so that we can obtain a reliable S velocity model and a reasonably good Moho depth model. Our preferred model was obtained with σ_β = 0.225 km/s and σ_H = 7.5 km. We use the least squares algorithm LSQR [*Paige and Saunders*, 1982a, 1982b] to solve equation (2).

3.1. Model Appraisal and Resolution Test

[16] One way to appraise an inverted model is showing the fits and/or root-mean-square (RMS) differences between observed and predicted data. Though our final model is based on the joint inversion of the fundamental mode group velocities and waveforms, for comparison purposes, we also carried out independent inversions of group velocity and of waveforms. Some results of these inversion tests are shown in the later sections. Hereinafter, we adopt the abbreviation DSP, PWI and JOINT to represent independent inversion of dispersions, independent inversion of waveforms and their joint inversion, respectively.

[17] Figure 3 shows an example of the observed and predicted group velocity dispersion curves of different models. Figure 3 (left) is a comparison among the predicted dispersions of the DSP, PWI and JOINT models. The three inverted models can fit the observed dispersions very well. Figure 3 (right) shows the improvement of the JOINT model in fitting the dispersion curves compared to the reference model SA40. Similarly, Figure 4 shows an example of waveform fits of different models. Figure 4 (top) is a comparison of the predicted waveforms of the DSP, PWI and JOINT models. Both the PWI and JOINT models fit the observed waveforms fairly well and better than the DSP model. Figure 4 (bottom) shows the improvement of the JOINT model to match the waveforms compared to the reference SA40 model. From many examples such as shown in Figures 3 and 4, we found that the model inverted only with dispersion constraints (DSP) cannot fit waveform data as well as the PWI and JOINT models, and that the model

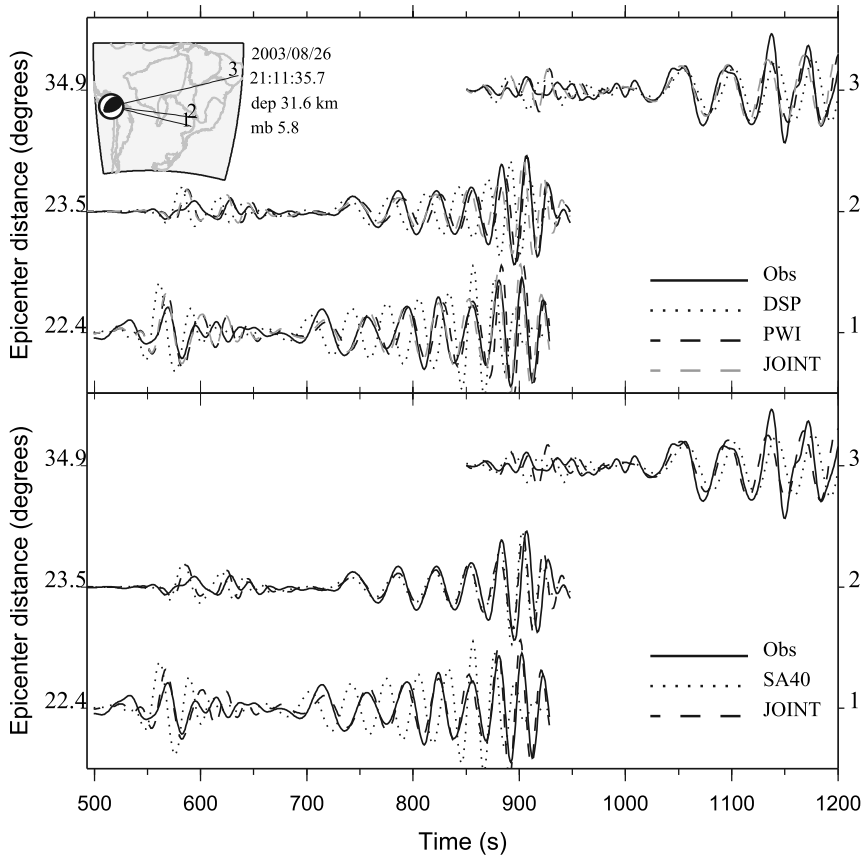

Figure 4. Fits between the observed and predicted waveforms of different models. (top) Comparison of the waveform fits among the DSP, PWI, and JOINT models. (bottom) Comparison of waveform fits between the JOINT and SA40 models.

inverted only with waveform constraints (PWI) gives worse group velocity fits compared to the DSP and JOINT models, as expected. The model inverted both with group velocities and waveforms (JOINT) fits both the dispersions and waveforms reasonably well. These results are quantified in Figures 5 and 6.

[18] Figure 5 shows RMS misfit of group velocity for different models. For periods longer than 50 s, the DSP model gives the lowest residuals, as expected. The PWI model gives higher RMS misfit than the DSP model, but significantly below the SA40 global average. The JOINT model gives very similar RMS misfit to the DSP model. For periods shorter than 50 s, the DSP model gives unexpected higher RMS misfit than the other two models. This may be due to the parameterization difference mentioned in the above section since group velocity partial derivatives are

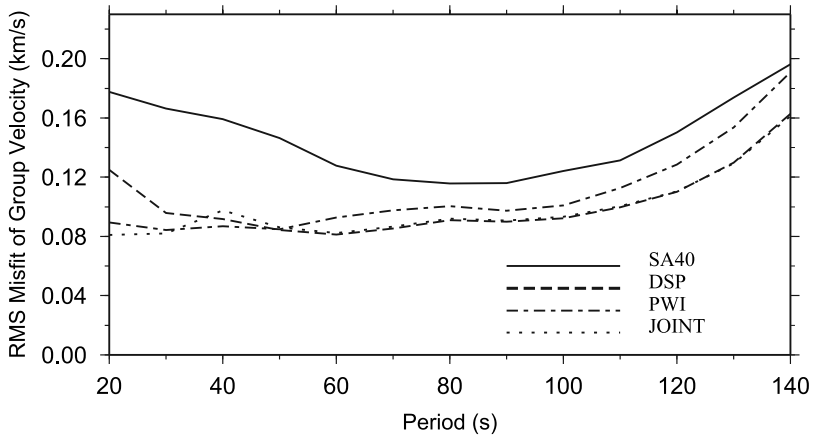

Figure 5. Root-mean-square (RMS) deviation between observed and predicted group velocities of the DSP, PWI, JOINT, and SA40 models.

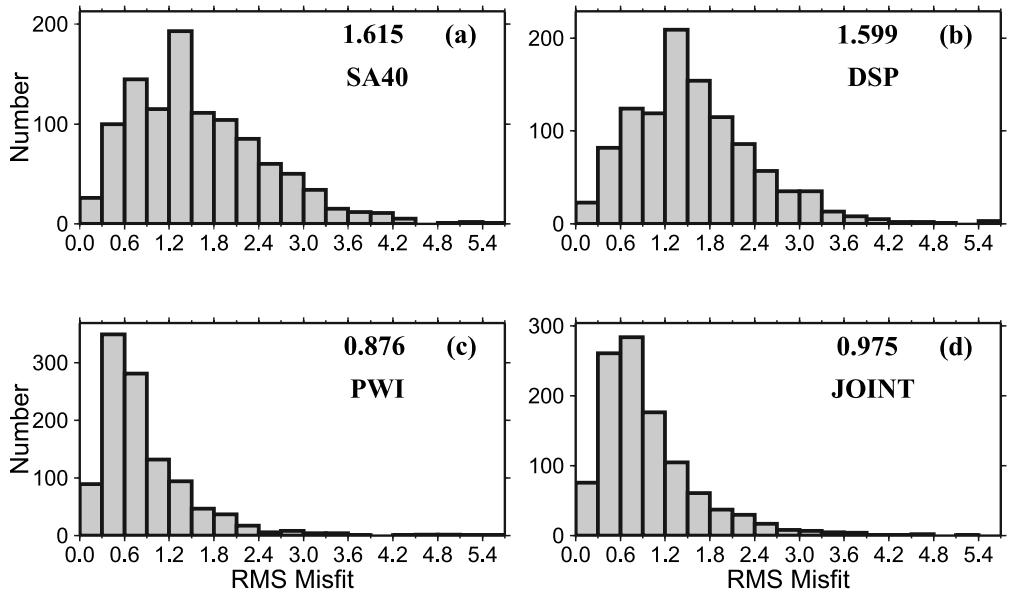

Figure 6. RMS deviation between observed and predicted waveforms of the DSP, PWI, JOINT, and SA40 models. The value on the top right of each panel is the mean RMS value.

initially calculated for geographically distributed layered models with vertical spacing of 20 km, while in the 3-D inversion, the 20 km layered model needs to be converted to the 3-D Cartesian model with 50 km vertical spacing, same as that used in PWI and JOINT. However, surface waves of short periods (<50 s) are mainly sensitive to depths shallower than 50 km, so the inverted model with 50 km vertical spacing is too coarse to fit short-period group velocities. Anyway, the present work mainly concerns about the upper mantle *S* velocities but not crustal structures. The JOINT model seems less influenced by the parameterization difference and gives about 40% reduction of RMS misfit relative to the SA40 model.

[19] Figure 6 shows the RMS misfit of waveforms for different models. Again, as expected, the PWI model gives least RMS misfit (fits best the observed waveforms). The JOINT model has RMS misfit only slightly higher (0.975) than the PWI model (0.876) but quite smaller than the DSP model (1.599). The JOINT model also produces about 40% of waveform RMS misfit reduction relative to the SA40 model. Figures 5 and 6 show that the model from the joint inversion fits the group velocities almost as well as the DSP model and also fits the waveforms almost as well as the PWI model.

[20] Tests with synthetic models are helpful to show the lateral and vertical resolving power of our model. For the *S* velocity resolution test, the input model was a checkerboard with $6^\circ \times 6^\circ$ cells and 200 km in depth with *S* velocities varying by ±7% relative to the iasp91 model, and Moho depths the same as the iasp91. Two sets of such checkers with contrary sense of anomaly are centered at 100 km and 300 km depths, respectively. For the Moho resolution test, the input model was a checkerboard with Moho depths varying by ±10 km relative to the Moho depths of the reference model, and *S* velocity the same as the iasp91. Random noises were added to the synthetic dispersions and waveforms. In each test, the inversion was carried out for both *S* velocity and Moho depth. Results of the resolution tests are shown in Figures 7b, 8, and 9. Figure 7b is the retrieved Moho depth from the JOINT test inversion. The amplitudes of the anomalies in the retrieved Moho model are underestimated in various amounts and least in the joint inversion. Limitation in data sensitivity and our resulting conventional preference for a smooth model precludes us capturing all of the steep gradients in the South American Moho. Our model thus provides regionally averaged Moho depth rather than local Moho depth. The retrieved model shows good spatial resolving power in the central part of the study region. Figure 8 shows horizontal slices of the retrieved *S* velocity models at 100 km and 300 km depths from inversions of DSP, PWI and JOINT. Both the retrieved DSP and PWI models showed good resolution at 100 km depth in the continent. The resolution of the JOINT model, however, is better than either the DSP or the PWI model alone. This can be seen along the northeastern margin of the continent where the dispersions and waveforms have quite different paths coverage. The PWI model still shows resolution in the central part at 300 km depth, while the DSP model has no resolution at this depth at all. The JOINT model incorporated the advantages of the DSP and PWI models, and gives good resolution down to ~200 km. At 300 km depth, features in the central continent are still interpretable because of the higher modes in the waveforms. Figure 9 shows three retrieved *S* velocity cross sections from the JOINT resolution test, crossing different regions (profile locations shown in Figures 1a and 10d). All the retrieved profiles resolved the input patterns reasonably well down to about 300–400 km but with resolving power decreasing with depth. As expected, profiles with denser paths coverage (e.g., profile aa') resolve the input pattern better than the profiles with poorer path coverage (e.g., profile cc').

4. Results and Discussions

[21] Our JOINT inverted model consists of Moho depth (Figure 7c) and 3-D upper mantle *S* velocity (Figures 10 and 11) of South America.

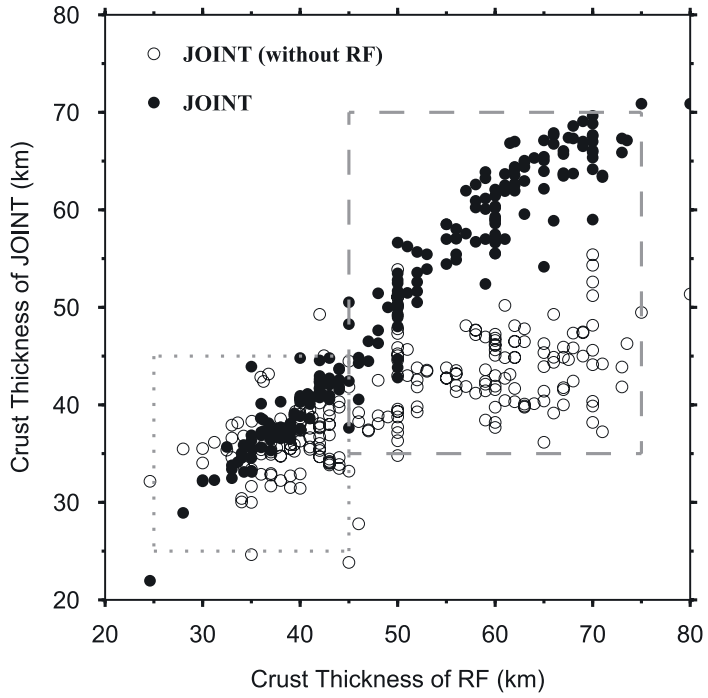

(a)

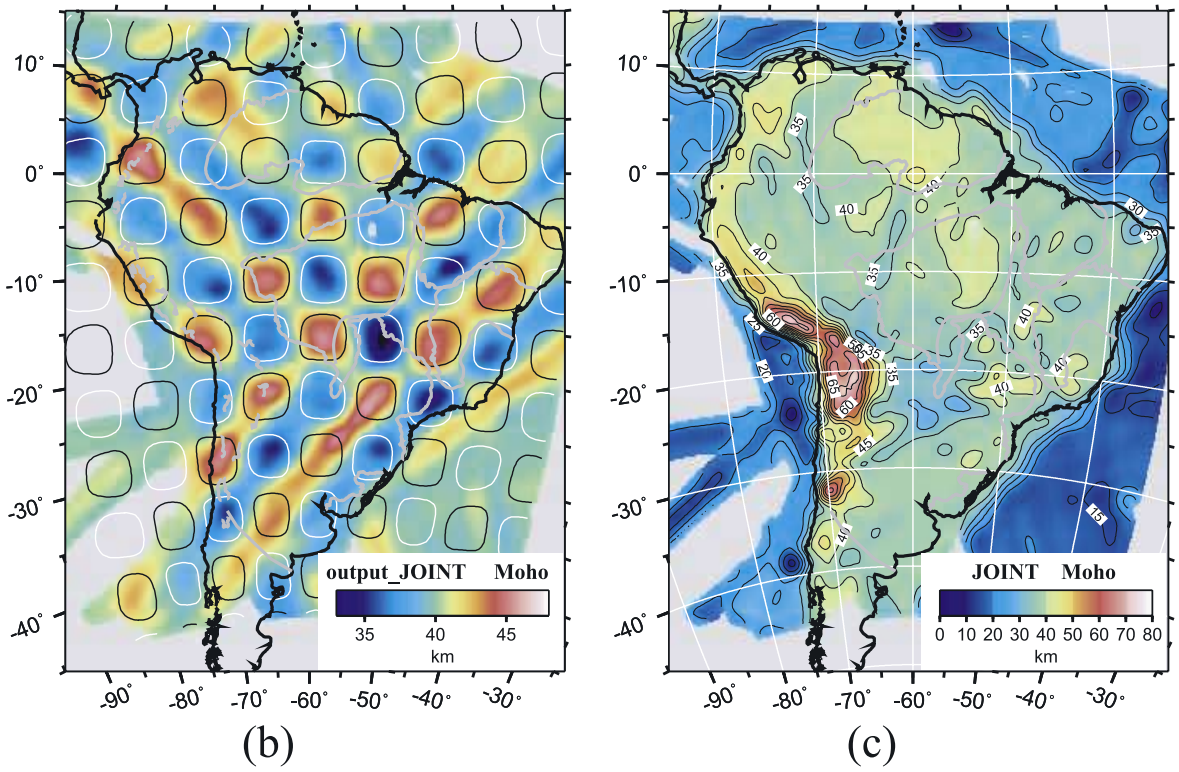

(b) (c)

Figure 7. (a) Crust thickness from joint inversion models versus crust thickness of the 229 a priori point constraints used in the final joint inversion. White circles are for the joint inversion without any point constraints, and black circles are for the final joint inversion (with point constraints). The dotted and dashed gray lines contain the crustal thicknesses of the stable continent (thickness <45 km) and the Andes Cordillera (thickness >45 km), respectively. (b) Retrieved Moho depth model from the JOINT resolution test inversion. The white and black lines represent the contours of −4 km and +4 km depth anomalies of the input model, respectively. (c) Moho depth model obtained in the present study. Contours are every 5 km.

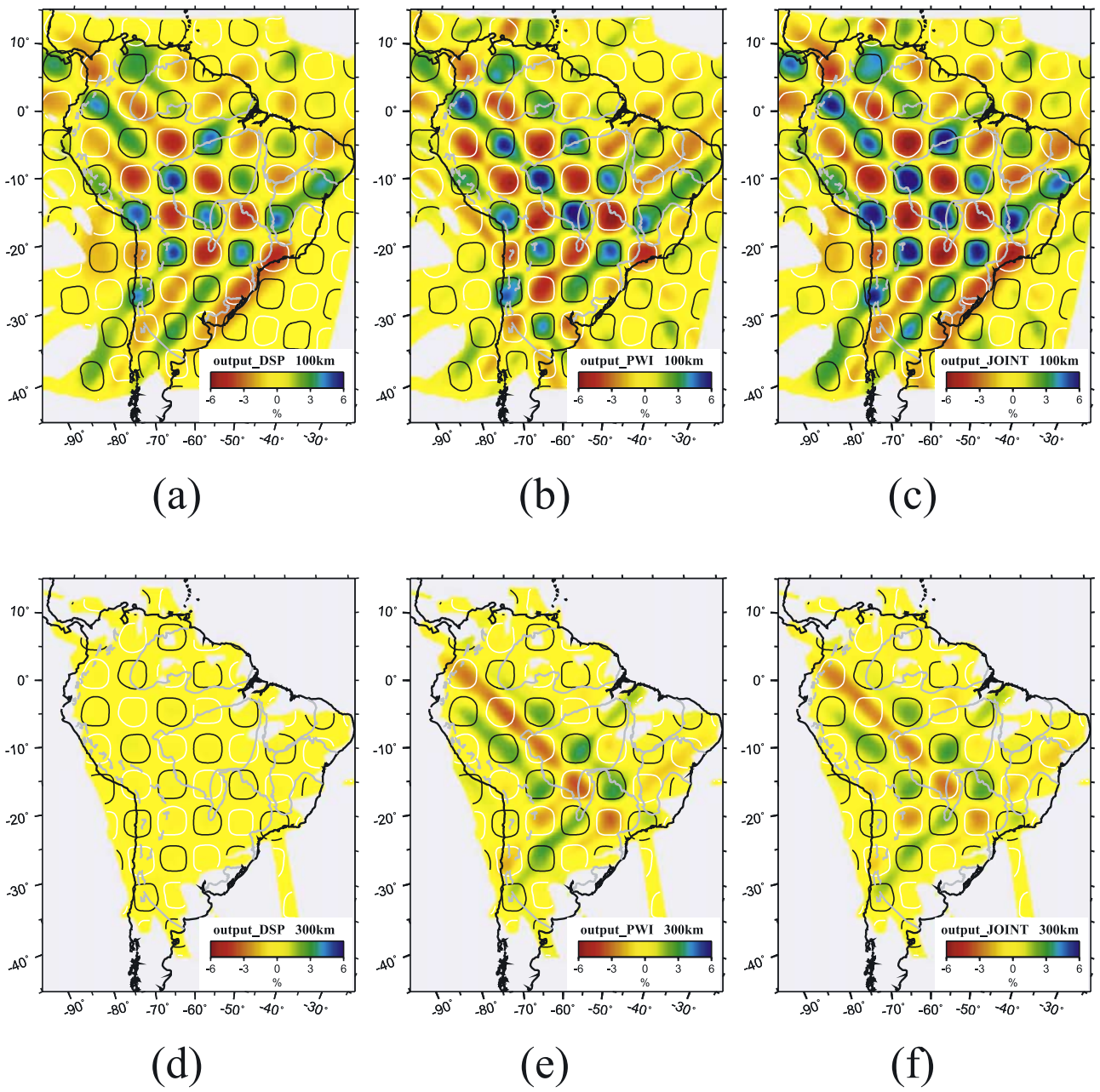

Figure 8. Horizontal slices at (a–c) 100 km and (d–f) 300 km for the retrieved *S* velocity models from the DSP (Figures 8a and 8d), PWI (Figures 8b and 8e), and JOINT (Figures 8c and 8f) resolution test inversions. The input model is represented by the white and black contours at −3.5% and 3.5% of *S* velocity perturbations, respectively.

4.1. Moho Depths

[22] Our continental Moho model (Figure 7c) shows stronger heterogeneity of crustal thickness than SA99 and the results based on extrapolated crustal types used for South America in model CRUST2.0 (G. Laske et al., CRUST2.0: A new global crustal model at 2° × 2°, 2000). Figure 7a illustrates the importance of our use of 229 independent point constraints on crustal thickness, mostly from receiver function studies, in the joint inversion. The inclusion of point constraints forces the model to be compatible with independent observations of crustal thickness, thereby reducing the trade-off with *S* velocity. The regions with point constraints (white circles in Figure 1a) therefore have smaller uncertainties. Figure 7a also shows that without including these point constraints, our joint inversion yields generally underestimated crustal thickness, especially for the Andean region. The underestimation of the extreme spatial variations in crustal thickness typical for South America is expected from the regularization of our inverse problem. Using external constraints on crustal thickness reduces the bias of potentially incorrect Moho on uppermost mantle *S* velocities.

[23] Our Moho depth estimates (Figure 7c) range from a minimum of 30 km in the central Chaco basin to depths of

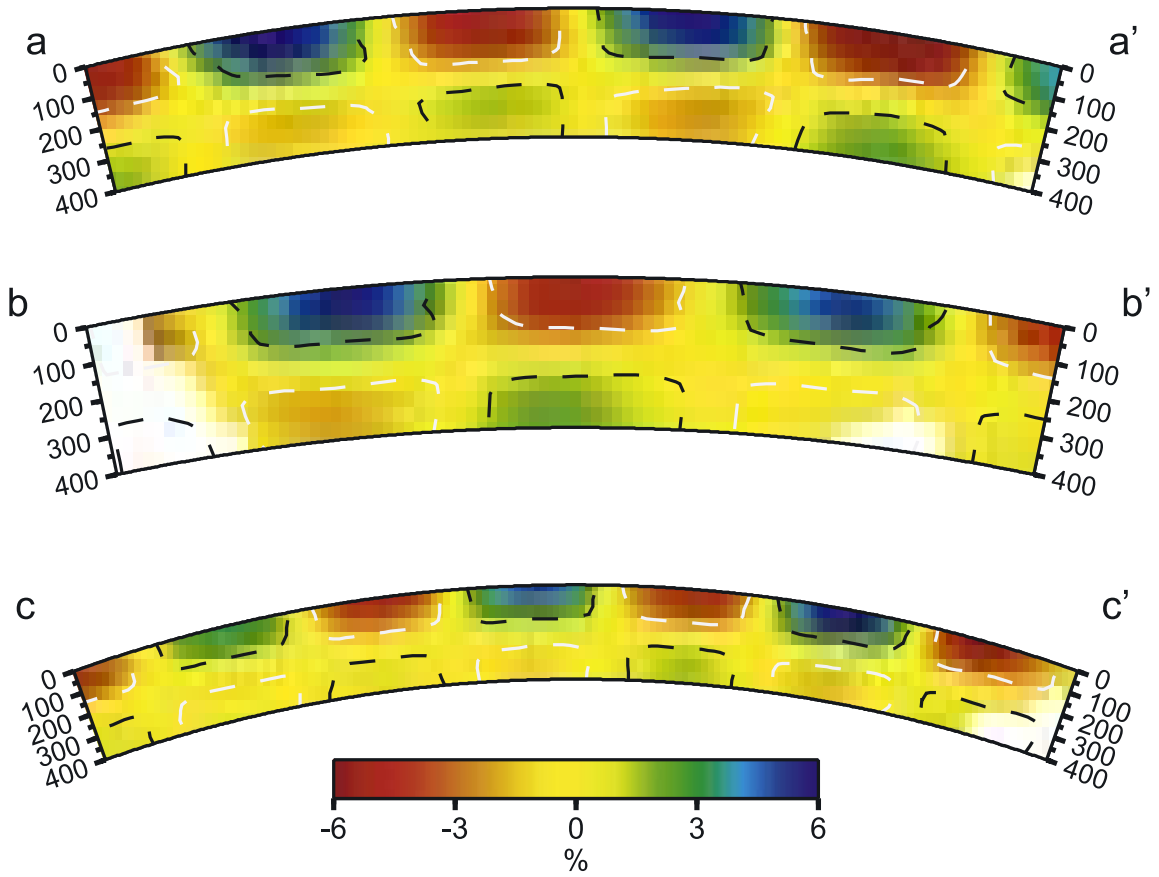

Figure 9. Three vertical profiles (location in Figures 1a and 10d) across the retrieved *S* velocity model from the JOINT resolution test inversion. The −3.5% and 3.5% perturbations in the input model are indicated by the white and black dashed contours, respectively. Regions with little to no resolution are white.

42 km beneath the Amazonian craton, and 45–70 km beneath the orogenic Andean belt. These values are partly constrained by receiver functions and seismic refraction/reflection studies [*An and Assumpção*, 2004; *Assumpção et al.*, 2004a, 2002; *Crotwell and Owens*, 2005; *França and Assumpção*, 2004; *Krüger et al.*, 2002; *Matos*, 1992; *Schmitz et al.*, 1999; *van der Lee et al.*, 2001; *Yuan et al.*, 2000]. Different from the extrapolated model 3SMAC [*Nataf and Richard*, 1996], the Amazon basin, does not show an overall thinner crust than the shields north and south of it. Beneath the northern Paraná basin the Moho is deeper than the surrounding fold belts, a result well constrained by the receiver functions from *França and Assumpção* [2004] and from *An and Assumpção* [2006, 2004]. Interestingly, a similar thickening is suggested for the Parnaíba basin in NE Brazil. In the oceans the resolving power (Figure 7b) is poor as we have neither point constraints, nor group velocity constraints and the Moho depth is mainly constrained by presumed isostatic equilibrium in addition to poor coverage waveform data.

4.2. Subduction Zone

[24] High *S* velocities are located beneath the three subhorizontal flat subduction zones in northern Colombia (8°N, 75°W), western Peru (from 5°S, 78°W to 10°S, 75°W), and central Chile (30°S, 69°W) at 100 km depth. These high-velocity segments correspond remarkably well to low heat flow areas in the Andes [*Hamza and Muñoz*, 1996; *Hamza et al.*, 2005]. Moderately high velocities have also been imaged parallel to the Andes from 0° to 30°S at depths of 150–200 km in several regions, reflecting the expected location of the subducting Nazca lithosphere. However, these high velocities are not continuous, mainly due to strong resolution variation for the subducting lithosphere since our data are mostly concentrated on the continental side of the Wadati-Benioff zone (Figure 2).

[25] Profile bb' (Figure 11) is a cross section through the Peruvian Andes and the western Amazon basin. High-velocity correspondent to the Peruvian flab slab [*Cahill and Isacks*, 1992] is not clearly imaged in this profile due to the poor resolution below the Wadati-Benioff zone (Figure 9). However, the Peruvian flab slab is visible on our 100 km horizontal slice map (Figure 10a).

[26] Extremely low *S* velocities are observed around 100 km in the mantle wedge beneath the Altiplano and eastern Cordillera of the Andes (13–27°S). With increasing depth (150–200 km), the low velocities beneath the highest Andean topography shift to the east and northeast to the foreland Chaco basin, the Pantanal and northwestern part of the Paraná basins (anomaly in the central part of the continent, on the 150–200 km maps, Figures 10b and 10c).

[27] A better view of this feature is shown in profile aa' in Figure 11, starting in the central Andes where the slab dips about 30° [*Cahill and Isacks*, 1992; *Ramos*, 1999]. On

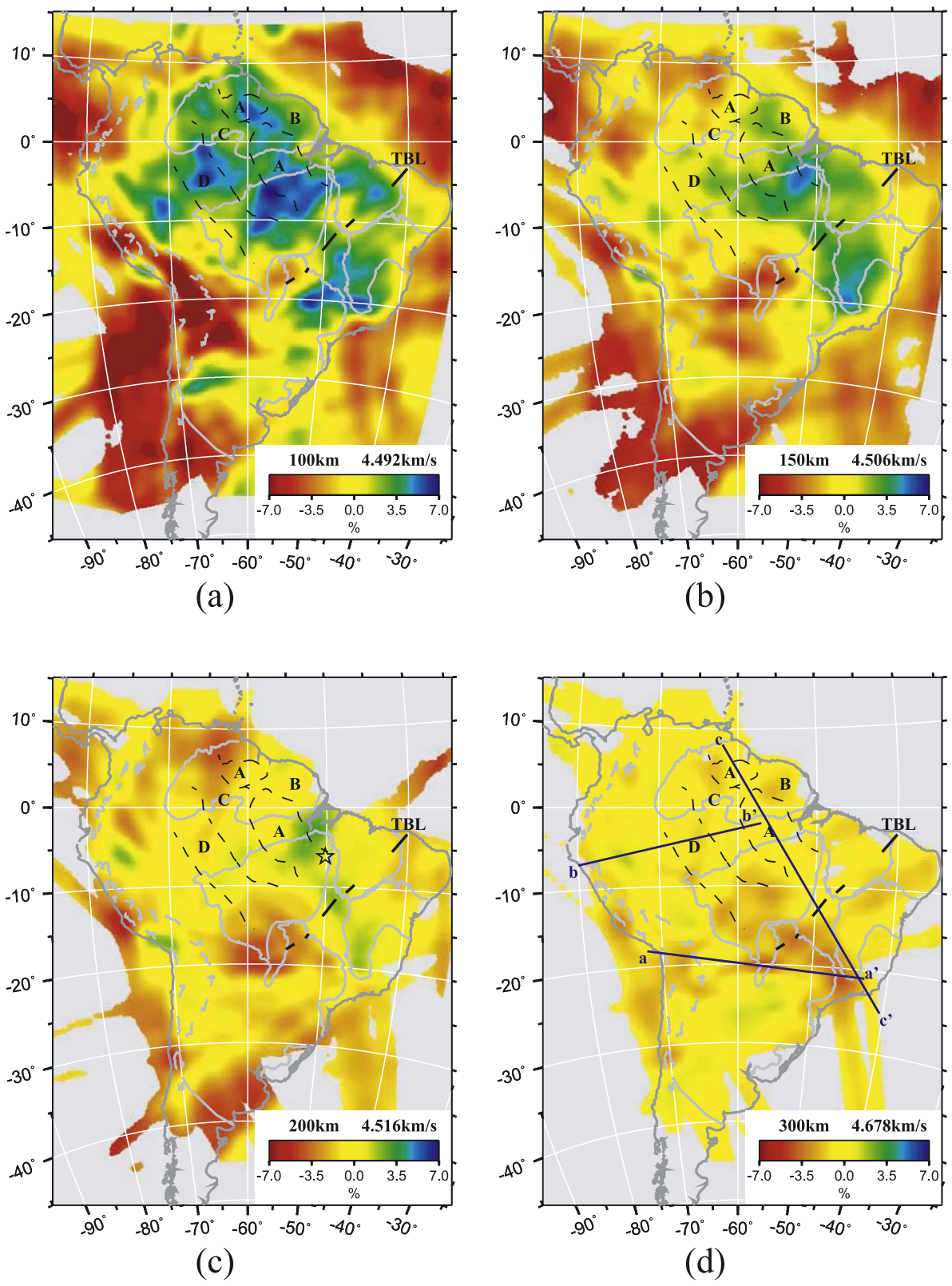

Figure 10. Horizontal slices of the obtained *S* velocity model at 100, 150, 200, and 300 km. The *S* velocities are mapped as deviations from those in iasp91. The dashed domains indicate the geochronological provinces of the Amazonian craton, where "A" is equivalent to the CAP (oldest domain), "B" to "MIP", "C" to VTP, and "D" to RNJP (youngest domain) in Figure 1b. RSIP and SP are too small to be shown here. TBL denotes the Transbrasiliano lineament. The star on the 200 km map indicates the location where the oldest rocks (2.9–3.0 Ga granitoids/greenstones) found in the Amazon craton. The aa, bb', and cc' on the 300 km map are the same profiles shown in Figure 1a.

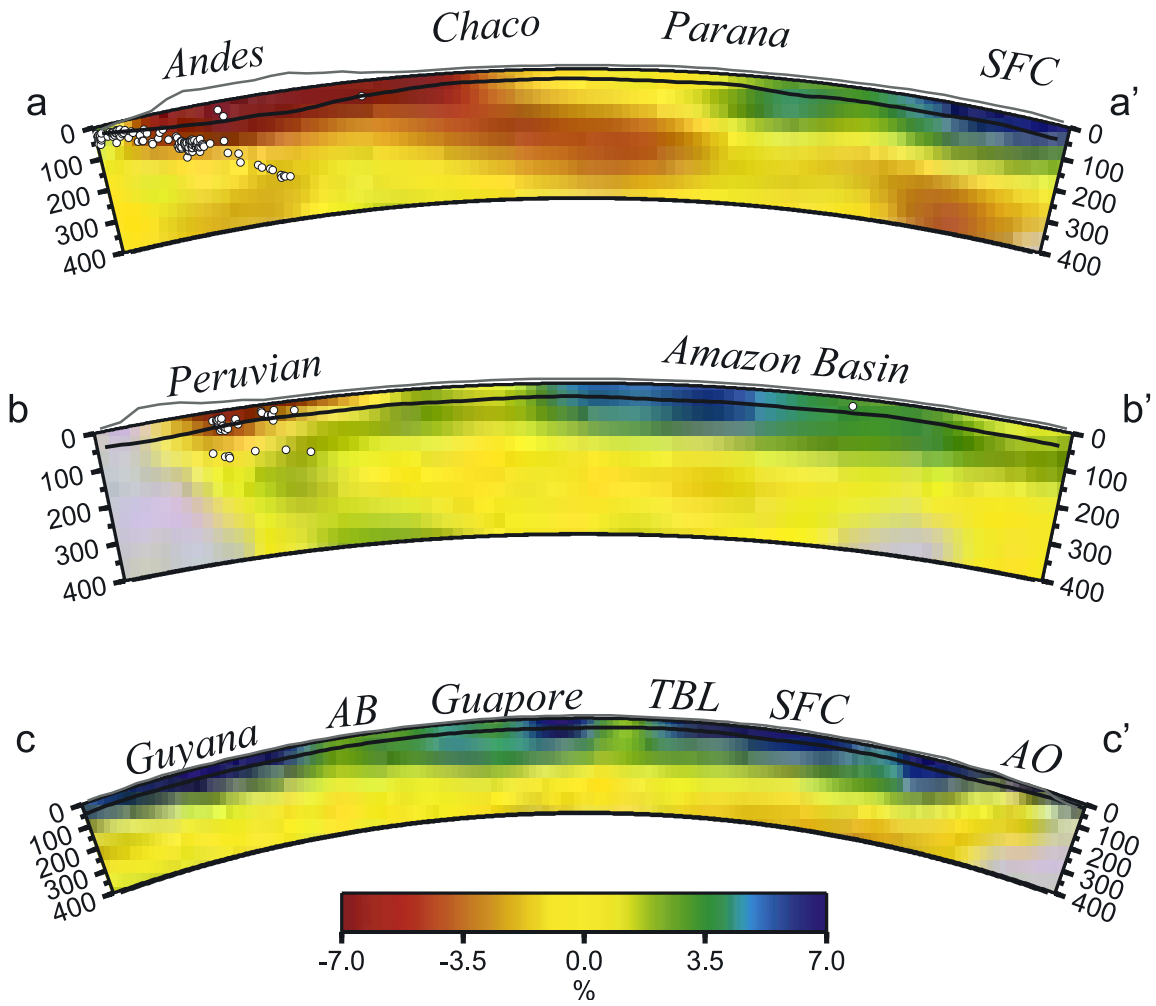

Figure 11. Same three vertical profiles as in Figure 10 but across the *S* velocity model obtained in the present study. Gray thin line is the exaggerated surface topography; thick line is the Moho discontinuity. Labels near the surface are AB, Amazon basin; TBL, Transbrasiliano lineament; SFC, São Francisco craton; and AO, Atlantic Ocean.

profile aa', the strong low-velocity anomaly beneath the Andes and the significantly weaker low-velocity anomaly beneath the Chaco and western Paraná basins forms a continuous unit, suggestive of a large-scale low-velocity zone beneath a relatively weak or thin lithosphere [*Assumpção et al.*, 2004a]. Model SA99 [*van der Lee et al.*, 2001] imaged two separate low-velocity anomalies, a strong one in the mantle wedge beneath the Andes and another, weaker anomaly beneath the Chaco and Pantanal basins. They inferred partial melting induced by water released from the subducting Nazca crust to explain the relatively strong low velocities in the mantle wedge, as compared to the weaker subplatform low velocities. *van der Lee et al.* [2001] further argued for diffuse influx of subplatform mantle into the mantle wedge, consistent with our joint model showing the low velocities to extend at least as deep as 400 km. Alternatively, the low velocities in profile aa' (Figure 11) could be interpreted as diffuse outflux out of the mantle wedge in an ENE direction, relative to the overlying rigid South America lithosphere, consistent with the motion of the Nazca plate relative to the South American continent [*Gripp and Gordon*, 2002]. If the latter alternative is correct, this low-velocity zone implies that the South America plate is no thicker than its high-velocity lithosphere and that little continental mantle is dragged down with the subducting Nazca plate toward the transition zone, possibly consistent with a decoupling effect of water between the slab and South American mantle at mantle wedge depths.

4.3. Precambrian Cratons

[28] Most of the northeastern continent (east of 70°W and north of 20°S) is underlain by high *S* velocities (Figure 10). High velocities down to 150–200 km (Figure 10) are likely associated with old and stable lithosphere of the Amazonian and São Francisco cratons.

[29] In contrast with the regional model of *Heintz et al.* [2005], our model does not show a basin-wide reduced anomaly beneath the Amazon basin, between the Guyana shield to the north and Guaporé shield to the south. Although some reduced anomalies are observed in the upper mantle of the eastern part of the basin, high velocities are observed beneath the western part (Figure 10a). Recent

estimates of effective elastic thicknesses (*Te*) in South America by spectral correlation of topography and Bouguer anomalies [*Pérez-Gussinyé et al.*, 2006] show that the eastern part of the Amazon basin tends to have low *Te* (<70 km) whereas the western part is characterized by large *Te* (>70 km) similar to the Guaporé shield, consistent with our results. This implies that the Amazonian lithosphere was not entirely affected by the rifting events during the basin evolution. In particular, our *S* velocities in the Amazonian craton (labels with "A–D" in Figure 10) seem to correlate with the geochronological provinces (Figure 1b) [*Tassinari and Macambira*, 1999]. For example, the depth extent and amplitude of the high velocities beneath the younger western Amazonian craton ("C" and "D") are smaller than beneath the older eastern craton ("A" and "B"). The imaged high *S* velocities in the northeastern Guaporé shield suggest a lithosphere about 200 km thick in this region, with the deepest root near the area (labeled by the star in Figure 10c) where the oldest Archean granitoids are found in the South American continent [*Sial et al.*, 1999]. The location of the highest velocities, at 200 km depth, in the northeastern part of the Guaporé shield is consistent with the model of *Heintz et al.* [2005].

[30] Most previous tomographic models [*Ritzwoller et al.*, 2002; *Silveira and Stutzmann*, 2002; *Silveira et al.*, 1998; *Vdovin et al.*, 1999] imaged a single high-velocity block beneath the Amazonian and the São Francisco cratons. In our model, the São Francisco craton is clearly separated from the Amazonian craton. A belt of lower velocities (thinner lithosphere) between the two cratons, at 100–200 km depths, roughly parallels the Transbrasiliano lineament. At the SW end of the TBL, low velocities beneath the Pantanal and Chaco basins (Figures 10a–10c) coincide with low *Te* [*Pérez-Gussinyé et al.*, 2006], high attenuation in the upper mantle (estimated from ScS2/ScS spectral ratios by M. B. Bianchi, and M. Assumpção (Strong *S* wave attenuation (low-Q) in the upper mantle under the Chaco and Pantanal basins using ScS2/ScS spectral ratios, unpublished manuscript, 2006)) and some indication of high heat flow anomalies [*Hamza et al.*, 2005]. Despite the large uncertainties in inferring upper mantle temperatures from shallow heat flow measurements, all the observations above are consistent with a thin lithosphere and strong asthenosphere separating the Amazonian domain to the NW and the São Francisco craton and Paraná basin domain to the SE.

[31] The Archean block in the southern part of the São Francisco craton is well defined by high *S* velocities down to about 150–200 km (Figures 10b and 10c). High velocities at 100 to 150 km depth extend from the São Francisco craton westward beneath the Brasília belt. *P* wave tomography and receiver function studies [*Assumpção et al.*, 2004b] are also consistent with a continuation at depth of the São Francisco craton beneath the low-grade metamorphic domain of the Brasília belt. These high *S* velocities are still visible on the 200 km map but are not as strong as in the Amazonian craton, implying that the lithospheric root of the Amazonian craton might be deeper than the São Francisco craton. Our tomography model shows a thicker lithospheric root beneath the southern part of the São Francisco craton, compared to its northern part. Interestingly, this "keel" structure may deflect the asthenospheric flow due to the absolute plate motion, as proposed by *Assumpção et al.* [2006] to explain the pattern of SKS splitting caused by upper mantle anisotropy.

[32] Profile cc' in Figure 11 is a cross section from the Amazonian craton in the northwest to the São Francisco craton in the southeast. High velocities have been imaged all along the profile but with different depth extent. Two relatively weaker high velocities along the profile cc' seem related to the eastern part of the Amazon basin (as discussed above) and the Transbrasiliano lineament. The northwestern part of the profile, at the Guyana shield, shows high velocity down to about 150 km, while the high velocity in the center of the profile (beneath the Guaporé shield) extends down to ~200 km. In the southeastern part (beneath the São Francisco craton), the high velocity extends to ~160 km. Our model shows a lithosphere of 160 km on average beneath the Amazonian and São Francisco cratons. The depth extent and velocity anomaly of the cratonic lithosphere in our model are not as large as for the lithosphere of the North American craton [*van der Lee and Frederiksen*, 2005; *van der Lee and Nolet*, 1997]. The South America cratons appear to be about 50 km thinner, which is in agreement with global-scale observations [*Grand*, 1994]. However, a similar difference was inferred between the predominantly Archean Canadian Shield and the predominantly Proterozoic platform to its south [*van der Lee and Frederiksen*, 2005]. With the South American cratons being predominantly Proterozoic in age, our results thus confirm the notion that Proterozoic lithosphere is thinner and less rigid than older Archean lithosphere. This difference in thickness makes sense if the lithosphere represents cold mantle depleted in crust-forming iron-rich melt, given that Archean conditions were more conducive to melting than Proterozoic conditions. In addition, this difference in lithospheric thickness between the two continents suggests that the lateral extent of a craton might be correlated with its depth extent.

4.4. Intracratonic Basins

[33] *Heintz et al.* [2005] inferred the Amazon Basin mantle lithosphere to be slower than the mantle of the surrounding Guyana and Guaporé shields. However, in our model the Amazon basin is underlain by generally high velocities, similar to the shields (Figures 10a and 10b). This discrepancy may be partly due to differences in Moho modeling between the two models.

[34] Also the Paraná and the Parnaíba basins appear to be underlain by high velocities to 100–150 km (Figures 10a and 10b). On the basis of radiometric dates from two basement samples, and the geometry of the surrounding fold belts, a Proterozoic "cratonic" nucleus has been inferred beneath the Paraná basin [*Cordani et al.*, 1984]. The high *S* velocities below the northern half of the basin are consistent with this hypothesis. On the other hand, *Milani and Ramos* [1998] show evidences of a rift zone in that part of the basin (determined by geophysical data) as well as early igneous activity which are not consistent with a completely stable cratonic nucleus. Our results indicate that any rifting episode during the evolution of the basin was not strong enough to affect the thick lithosphere on a regional scale detectable by our surface wave tomography. High *S* velocities are further imaged beneath the Parnaíba basin in NE Brazil (Figure 10a), where a cratonic nucleus has also been

proposed [*Cordani et al.*, 1984]. This compares well with North America where most intracratonic basins also appear to be on high-velocity mantle [*van der Lee and Frederiksen*, 2005; *van der Lee and Nolet*, 1997]. Interestingly, the lithospheric flexural rigidity in the Parnaíba and Paraná basins seem to be as high as in the cratonic areas [*Pérez-Gussinyé et al.*, 2006].

[35] At 300 km depth, a low *S* velocity anomaly (about −3.5%) is located in the northern Paraná basin and just south of the São Francisco craton (Figures 10d and 11a). The resolution tests (Figures 8f and 9a) show good resolving power down to 400 km in this region. This low-velocity is first detected with body wave tomography and was speculated to represent a fossil plume [*Schimmel et al.*, 2003; *VanDecar et al.*, 1995]. The thermal nature of the anomaly has been disputed by *Liu et al.* [2003], who mapped the topography of the 410 and 650 km discontinuities and found no evidence for a significant temperature anomaly beneath SE Brazil. Our results confirm the existence of a large volume with strong low velocities but do not resolve details necessary to resolve the dispute.

4.5. Oceanic Regions

[36] The oceanic regions of our model have too limited resolving power (Figure 8) to permit a detailed interpretation. However, resolution tests with larger checkerboard size (not shown here) can retrieve large-scale features of about 10°. On average the *S* velocities of the south Atlantic and east Pacific oceans covered by our model show a lithosphere less than ∼100 km thick, more than 50 km shallower than the cratonic lithosphere of the continent. The eastern Pacific Ocean has lower *S* velocity than the western Atlantic Ocean in the uppermost upper mantle depths. Similar velocity contrasts were determined by *Heintz et al.* [2005]. This difference is probably related to the contrasting ages of the oceanic lithospheres. The fast spreading rates of the Pacific ridge [*Gripp and Gordon*, 2002] carried younger and thinner oceanic lithosphere to the eastern Pacific Ocean compared to the western Atlantic Ocean.

5. Conclusions

[37] A wide collection of broadband seismograms recorded by the global permanent, densified in South America over the past decade, and regional temporary stations, augmented by the newly deployed BLSP array, provides the best wave path coverage to date for the stable continent, especially for the Amazonian craton. A new joint inversion method based on the partitioned waveform inversion and two-step group velocity tomography is developed to simultaneously invert regional wave trains and fundamental mode group velocities. The method is applied to 5700 group velocity curves and 1537 regional waveforms to produce the Moho and 3-D upper mantle *S* velocity model for South America. Our model has improved depth and lateral resolution due to the inclusion of higher-mode waveform data and the excellent path coverage. Also, our upper mantle *S* velocity model is less affected by crustal uncertainties because the Moho depth is simultaneously inverted for. Our results confirm the following features presented in earlier models: (1) High-velocity lithosphere is found beneath the Amazonian and São Francisco cratons. (2) Extremely low velocities are imaged in the mantle wedge beneath the highest topography of the Andes. (3) Low velocities are found beneath the Chaco, Pantanal, and western Paraná basins. (4) Flat subduction slabs along the Andes are characterized by moderately high *S* velocity and the absence of a low-velocity mantle wedge. (5) The main new features imaged in our model are as follows:

[38] 1. Crustal thicknesses in the Amazon basin are not smaller than in the Guyana and Guaporé shields.

[39] 2. Generally high velocities are observed beneath the most of the Amazon basin and part of the Paraná and Parnaíba basins in the depth of 100–150 km. In the Amazon basin, velocities in the 100–150 km depth are generally similar to those in the two shields north and south of it.

[40] 3. Lithosphere in the Amazonian craton has an overall average thickness of around 160 km, with the eastern Archean part being faster and thicker (∼200 km) than the western part of the craton, generally consistent with the younging trend of the Precambrian geochronological provinces.

[41] 4. The Amazonian craton and the São Francisco craton, characterized by high upper mantle velocity, are separated by the Transbrasiliano lineament with a belt of lower velocities at 100–200 km depths.

[42] Our modeling of the South American mantle thus provides valuable information to global debates on the characteristics of continental lithosphere and asthenosphere, the nature of the mantle wedge above the subducting Nazca Plate, and the difference between Proterozoic and Archean lithosphere, continent-scale tectonics, and intracratonic basins. Our modeling also illuminates some of the potential causes or consequences of South American tectonics and dynamics. More specifically, the Transbrasiliano lineament might have had a larger influence on South American tectonics than the Amazon rift. Furthermore, the depth extent and anomaly strength of Precambrian lithosphere might not only be correlated with its age and corresponding inferred degree of melt depletion but also with the lateral extent of the craton. The latter could result from high velocities exhibited by the cratonic lithosphere being largely a result of its temperature. Last, our model adds to the enigma of the origin of intracratonic basins and rifts, and increases the global database of such basins that have no discernable mantle anomaly associated with them.

[43] **Acknowledgments.** This work was financed mainly by MCT Mineral Fund, Brazil, with additional support from FAPESP (grants 96/01566-0, 01/06066-6, 02/00244-2), CNPq (30.0227/79, 52.0078/00-4), and NSFC, China (grant 40504011). ETH-Z, Switzerland (grant 0-20990-02), provided financial support and seismic equipment for the field deployment (BLSP02 [*Feng et al.*, 2004]) from which most of the processed data are retrieved. Northwestern University's Arthur Howland Fund provided further support for van der Lee's travel to Brazil. We thank Federica Marone, Mark Van der Meijde, Peter Zweifel, Beat Rinderknecht, Andre Blanchard, Eduardo Mandel, José Roberto Barbosa, and Marcelo Bianchi for fieldwork and general support.

References

Almeida, F. F. M., B. B. B. Neves, and C. D. R. D. Carneiro (2000), The origin and evolution of the South American Platform, *Earth Sci. Rev.*, *50*, 77–111.

An, M., and M. S. Assumpção (2004), Multi-objective inversion of surface waves and receiver functions by competent genetic algorithm applied to the crustal structure of the Paraná Basin, SE Brazil, *Geophys. Res. Lett.*, *31*, L05615, doi:10.1029/2003GL019179.

An, M., and M. Assumpção (2006), Crustal and upper mantle structure in the intracratonic Paraná Basin, SE Brazil, from surface wave dispersion using genetic algorithm, *J. S. Am. Earth Sci.*, *21*, 173–184.

Assumpção, M., D. James, and A. Snoke (2002), Crustal thicknesses in SE Brazilian Shield by receiver function analysis: Implications for isostatic compensation, *J. Geophys. Res.*, *107*(B1), 2006, doi:10.1029/2001JB000422.

Assumpção, M. S., M. An, M. Bianchi, G. S. L. França, M. Rocha, J. R. Barbosa, and J. Berrocal (2004a), Seismic studies of the Brasília Foldbelt at the western border of the São Francisoco craton, central Brazil, using receiver function, surface wave dispersion, and teleseismic tomography, *Tectonophysics*, *388*, 173–185.

Assumpção, M. S., M. Schimmel, C. Escalante, J. R. Barbosa, M. Rocha, and L. V. Barros (2004b), Intraplate seismicity in SE Brazil: Stress concentration in lithospheric thin spots, *Geophys. J. Int.*, *159*, 390–399.

Assumpção, M., M. Heintz, A. Vauchez, and M. Egydio-Silva (2006), Upper mantle anisotropy in SE and central Brazil from SKS splitting: Evidence of asthenospheric flow around a cratonic keel, *Earth Planet. Sci. Lett.*, *250*, 224–240.

Beck, S. L., G. Zandt, S. C. Myers, T. C. Wallace, P. G. Silver, and L. Drake (1996), Crustal-thickness variations in the central Andes, *Geology*, *24*, 407–410.

Boschi, L., and G. Ekström (2002), New images of the Earth's upper mantle from measurements of surface wave phase velocity anomalies, *J. Geophys. Res.*, *107*(B4), 2059, doi:10.1029/2000JB000059.

Cahill, T., and B. L. Isacks (1992), Seismicity and the shape of the subducted Nazca plate, *J. Geophys. Res.*, *97*, 17,503–17,529.

Cordani, U. G., and K. Sato (1999), Crustal evolution of the South American Platform, based on Nd isotopic systematics on granitoid rocks, *Episodes*, *22*, 167–173.

Cordani, U. G., B. B. Brito Neves, R. A. Fuck, R. Porto, A. Thomas Filho, and F. M. B. Cunha (1984), Estudo preliminar de integração do pré-Cambriano com os eventos tectônicos das bacias sedimentares Brasileiras, *Bul. Cienc. Tec. Pet. Secao Explor. Pet.*, *70*.

Crotwell, H. P., and T. J. Owens (2005), Automated receiver function processing, *Seismol. Res. Lett.*, *76*, 702–708.

Dorbath, C., and F. Masson (2000), Composition of the crust and upper-mantle in the central Andes (19°30′S) inferred from P velocity and Poisson's ration, *Tectonophysics*, *327*, 213–223.

Dziewonski, A. M., A. Friedman, D. Giardini, and J. H. Woodhouse (1983), Global seismicity of 1982: Centroid-moment tensor solutions for 308 earthquakes, *Phys. Earth Planet. Inter.*, *33*, 76–90.

Ekström, G., and M. Dziewonski (1998), The unique anisotropy of the Pacific upper mantle, *Nature*, *394*, 168–172.

Engdahl, E. R., R. D. van der Hilst, and J. Berrocal (1995), Imaging of subducted lithosphere beneath South America, *Geophys. Res. Lett.*, *22*, 2317–2320.

Engdahl, E. R., R. D. van der Hilst, and R. Buland (1998), Global teleseismic earthquake relocation with improved travel times and procedures for depth determination, *Bull. Seismol. Soc. Am.*, *88*, 722–743.

Feng, M., M. S. Assumpção, and S. van der Lee (2004), Group-velocity tomography and lithospheric S-velocity structure of the South American continent, *Phys. Earth Planet. Inter.*, *147*, 315–331.

França, G. S. L., and M. S. Assumpção (2004), Crustal Structure of the Ribeira fold belt, SE Brazil, derived from receiver functions, *J. S. Am. Earth Sci.*, *16*, 743–758.

Goodwin, A. M. (1991), *Precambrian Geology*, Elsevier, New York.

Grand, S. P. (1994), Mantle shear structure beneath the Americas and surrounding oceans, *J. Geophys. Res.*, *99*, 11,591–11,622.

Gripp, A. E., and R. G. Gordon (2002), Young tracks of hotspots and current plate velocities, *Geophys. J. Int.*, *150*, 321–361.

Gutscher, M. A., and J. Malavieille (1999), Style of upper plate deformation linked to interplate coupling over flat slab segments: Evidence from the Andean Margin, in *Thrust Tectonics 99 London, Abstracts*, edited by K. McClay, pp. 214–217, Royal Holloway, London.

Haberland, C., and A. Rietbrock (2001), Attenuation tomography in the western central Andes: A detailed insight into the structure of a magmatic arc, *J. Geophys. Res.*, *106*, 11,151–11,167.

Hamza, V. M., and M. Muñoz (1996), Heat flow map of South America, *Geothermics*, *25*, 599–646.

Hamza, V. M., F. J. S. Silva Dias, A. J. L. Gomes, and D. T. Z. G. (2005), Numerical and functional representations of regional heat flow in South America, *Phys. Earth Planet. Inter.*, *152*, 223–256.

Heintz, M., E. Debayle, and A. Vauchez (2005), Upper mantle structure of the South American Continent and neighboring oceans from surface wave tomography, *Tectonophysics*, *406*, 115–139.

James, D. E., and J. A. Snoke (1990), Seismic evidence for continuity of the deep slab beneath central and eastern Peru, *J. Geophys. Res.*, *95*, 4989–5001.

James, D. E., M. S. Assumpção, J. A. Snoke, L. C. Ribotta, and R. Kuehnel (1993), Seismic studies of continental lithosphere beneath SE Brazil, *Ann. Acad. Bras. Cien.*, *65*, 227–250.

Kennett, B. L. N., and E. R. Engdahl (1991), Traveltimes for global earthquake location and phase identification, *Geophys. J. Int.*, *105*, 429–465.

Krüger, F., F. Scherbaum, J. W. C. Rosa, R. Kind, F. Zetsche, and J. Höhne (2002), Crustal and upper mantle structure in the Amazon region (Brazil) determined with broadband mobile stations, *J. Geophys. Res.*, *107*(B10), 2265, doi:10.1029/2001JB000598.

Larson, E. W. F., and G. Ekström (2001), Global models of surface wave group velocity, *Pure Appl. Geophys.*, *158*, 1377–1399.

Laske, G., and G. Masters (1996), Constraints on global phase-velocity maps from long-period polarization data, *J. Geophys. Res.*, *101*, 16,059–16,075.

Liu, K. H., S. S. Gao, P. G. Silver, and Y. Zhang (2003), Mantle layering across central South America, *J. Geophys. Res.*, *108*(B11), 2510, doi:10.1029/2002JB002208.

Matos, R. (1992), The northeast Brazilian rift system, *Tectonics*, *11*, 766–791.

Mégnin, C., and B. Romanowicz (2000), The shear velocity structure of the mantle from the inversion of body, surface and higher modes waveforms, *Geophys. J. Int.*, *143*, 709–728.

Milani, E. J., and V. A. Ramos (1998), Orogenias Paleozóicas no domínio sul-ocidental do Gondwana e os ciclos de subsidência da Bacia do Paraná, *Rev. Brasil. Geocienc.*, *28*, 473–484.

Mooney, W. D., G. Laske, and G. Masters (1998), CRUST5.1: A global crustal model at 5° × 5°, *J. Geophys. Res.*, *103*, 727–747.

Myers, S. C., S. Beck, G. Zandt, and T. Wallace (1998), Lithospheric-scale structure across the Bolivian Andes from tomographic images of velocity and attenuation for P and S wave, *J. Geophys. Res.*, *103*, 21,233–21,252.

Nataf, H. C., and Y. Richard (1996), 3SMAC: An a priori tomographic model of the upper mantle based on geophysical modeling, *Phys. Earth Planet. Inter.*, *95*, 101–122.

Paige, C. C., and M. A. Saunders (1982a), Algorithm 583, LSQR: Sparse linear equations and least squares problems, *Trans. Math. Software*, *8*, 195–209.

Paige, C. C., and M. A. Saunders (1982b), LSQR: An algorithm for sparse linear equations and sparse least squares, *Trans. Math. Software*, *8*, 43–71.

Pasyanos, M. E., W. R. Walter, and S. E. Hazler (2001), A surface wave dispersion study of the Middle East and North Africa for monitoring the Comprehensive Nuclear-Test-Ban Treaty, *Pure Appl. Geophys.*, *158*, 1445–1474.

Pennington, W. D. (1981), Subduction of the eastern Panama Basin and seismotectonics of northwest South America, *J. Geophys. Res.*, *86*, 10,753–10,770.

Pérez-Gussinyé, M., A. R. Lowry, A. B. Watts, and J. Phipps Morgan (2006), Tracing lithospheric structure using flexural rigidity in South America: Implications for intra-continental deformation and subduction geometry, *Eos Trans. AGU*, *87*(52), Fall Meet. Suppl., Abstract T51A-1518.

Ramos, V. A. (1999), Plate tectonic setting of the Andean Cordillera, *Episodes*, *22*, 183–190.

Ritsema, J., H. J. van Heijst, and J. H. Woodhouse (2004), Global transition zone tomography, *J. Geophys. Res.*, *109*, B02302, doi:10.1029/2003JB002610.

Ritzwoller, M. H., and A. L. Levshin (1998), Eurasian surface wave tomography: Group velocities, *J. Geophys. Res.*, *103*, 4839–4878.

Ritzwoller, M. H., N. M. Shapiro, M. P. Barmin, and A. L. Levshin (2002), Global surface wave diffraction tomography, *J. Geophys. Res.*, *107*(B12), 2335, doi:10.1029/2002JB001777.

Russo, R. M., P. G. Silver, M. Franke, W. B. Ambeh, and D. E. James (1996), Shear-wave splitting in northeast Venezuela, Trinidad, and the eastern Caribbean, *Phys. Earth Planet. Inter.*, *95*, 251–275.

Santos, J. O. S., L. A. Hartmann, H. E. Gaudette, D. I. Groves, N. J. Mcnaughton, and I. R. Fletcher (2000), A new understanding of the provinces of the Amazon Craton based on integration of field mapping and U-Pb and Sm-Nd geochronology, *Gondwana Research*, *3*, 453–488.

Schimmel, M., M. Assumpção, and J. C. VanDecar (2003), Seismic velocity anomalies beneath SE Brazil from *P* and *S* wave travel time inversions, *J. Geophys. Res.*, *108*(B4), 2191, doi:10.1029/2001JB000187.

Schmitz, M., et al. (1999), The crustal structure beneath the central Andean forearc and magmatic arc as derived from seismic studies the PISCO 94 experiment in northern Chile (21°–23°S), *J. S. Am. Earth Sci.*, *12*, 237–260.

Schmitz, M., D. Chalbaud, J. Castillo, and C. Izarra (2002), The crustal structure of the Guayana Shield, Venezuela, from seismic refraction and gravity data, *Tectonophysics*, *345*, 103–118.

Schneider, J. F., and I. S. Sacks (1987), Stress in the contorted Nazca Plate beneath southern Peru from local earthquakes, *J. Geophys. Res.*, *92*, 13,887–13,902.

Shapiro, N. M., and M. H. Ritzwoller (2002), Monte-Carlo inversion for a global shear-velocity model of the crust and upper mantle, *Geophys. J. Int.*, *151*, 88–105.

Sial, A. N., R. D. Agnol, V. P. Ferreira, L. V. S. Nardi, M. M. Pimentel, and C. M. Wiedemann (1999), Precambrian granitic magmatism in Brazil, *Episodes*, *22*, 191–198.

Silveira, G., and E. Stutzmann (2002), Anisotropic tomography of the Atlantic Ocean, *Phys. Earth Planet. Inter.*, *132*, 237–248.

Silveira, G., E. Stutzmann, D. A. Griot, J. P. Montagner, and L. M. Victor (1998), Anisotropic tomography of the Atlantic Ocean from Rayleigh surface waves, *Phys. Earth Planet. Inter.*, *106*, 257–273.

Tassinari, C. C. G., and M. J. B. Macambira (1999), Geochronological provinces of the Amazonian Craton, *Episodes*, *22*, 174–182.

Teixeira, W., P. Sabaté, J. R. Barbosa, C. M. Noce, and M. A. Carneiro (2000), Archean and Paleoproterozoic tectonic evolution of the Sao Francisco craton, Brazil, in *Tectonic Evolution of South America, 31st International Geological Congress, Rio de Janeiro, Brazil, August 6-17, 2000*, edited by U. G. Cordani et al., pp. 101–137, Fundo Setorial de Pet. e Gás Nat., Rio de Janeiro.

Trampert, J., and J. H. Woodhouse (1995), Global phase velocity maps of Love and Rayleigh waves between 40 and 150 seconds, *Geophys. J. Int.*, *122*, 675–690.

VanDecar, J. C., D. E. James, and M. Assumpção (1995), Seismic evidence for a fossil mantle plume beneath South America and implications for plate driving forces, *Nature*, *378*, 25–31.

van der Lee, S., and A. Frederiksen (2005), Surface wave tomography applied to the North American upper mantle, in *Seismic Earth: Array Analysis of Broadband Seismograms*, *Geophys. Monogr. Ser.*, vol. 157, edited by A. Levander and G. Nolet, pp. 67–80, AGU, Washington, D. C.

van der Lee, S., and G. Nolet (1997), Upper mantle *S* velocity structure of North America, *J. Geophys. Res.*, *102*, 22,815–22,838.

van der Lee, S., D. James, and P. Silver (2001), Upper mantle *S* velocity structure of central and western South America, *J. Geophys. Res.*, *106*, 30,821–30,834, (Correction to "Upper mantle *S* velocity structure of central and western South America," by Suzan van der Lee, David James, and Paul Silver, *J. Geophys. Res., 107*(B5), 2099, doi:10.1029/2002JB001891, 2002.)

Vdovin, O., J. A. Rial, A. L. Levshin, and M. H. Ritzwoller (1999), Group-velocity tomography of South America and the surrounding oceans, *Geophys. J. Int.*, *136*, 324–340.

Villaseñor, A., M. H. Ritzwoller, A. L. Levshin, M. P. Barmin, E. R. Engdahl, W. Spakman, and J. Trampert (2001), Shear velocity structure of central Eurasia from inversion of surface wave velocities, *Phys. Earth Planet. Inter.*, *123*, 169–184.

Woodhouse, J. H., and A. M. Dziewonski (1984), Mapping the upper mantle: Three-dimensional modeling of Earth structure by inversion of seismic waveforms, *J. Geophys. Res.*, *89*, 5953–5986.

Yuan, X., et al. (2000), Subduction and collision processes in the central Andes constrained by converted seismic phases, *Nature*, *408*, 958–961.

M. Assumpção, Department of Geophysics, IAG, University of São Paulo, Rua do Matão 1226, São Paulo, SP, 05508-090, Brazil. (marcelo@iag.usp.br)

M. Feng, Institute of Geomechanics, Chinese Academy of Geological Sciences, MinZuDaXueNanLu 11, 100081, Beijing, China. (mei_feng_cn@yahoo.com.cn)

S. van der Lee, Department of Geological Sciences, Northwestern University, Evanston, IL 60208, USA. (suzan@earth.northwestern.edu)